Modeling energetic electron penetration into the slot region and inner radiation belt

H. Zhao[1,2] and X. Li[1,2]

Received 22 July 2013; revised 16 October 2013; accepted 17 October 2013; published 5 November 2013.

[1] The inner radiation belt is thought to be quite stable, and only the most intense geomagnetic storms can cause energetic electron variations in the slot region and inner belt. In this paper, using energetic electron flux data from Detection of Electro-Magnetic Emissions Transmitted from Earthquake Regions (DEMETER) satellite, we show that 100s keV electron flux enhancements in the slot region and inner belt are seen quite often and can occur even during moderate geomagnetic storms. In addition, by transforming the energetic electron flux data into the phase space density (PSD), we model the inward radial transport of two different electron populations, μ = 30 MeV/G (K = 0) and μ = 15 MeV/G (K = 0), using a 1-D radial diffusion model in which the radial diffusion coefficient is directly associated with solar wind parameters and L shell. The model results reproduce the PSD data well in the slot region and inner belt, indicating that the flux enhancement in the inner belt and slot region can be well explained by inward radial transport. The radial diffusion coefficients used in our model are much larger than the widely used *Kp*-dependent electromagnetic radial diffusion coefficient but are smaller than the *Kp*-dependent electrostatic radial diffusion coefficient (Brautigam and Albert, 2000), suggesting that the *Kp*-dependent diffusion coefficient cannot be simply extended to lower L region to account for the observed enhancements of energetic electrons in the slot region and inner belt.

Citation: Zhao, H., and X. Li (2013), Modeling energetic electron penetration into the slot region and inner radiation belt, *J. Geophys. Res. Space Physics*, *118*, 6936–6945, doi:10.1002/2013JA019240.

1. Introduction

[2] Energetic electrons in the inner magnetosphere are distributed into two regions: the inner radiation belt and the outer radiation belt. The outer radiation belt is highly dynamic, while the inner radiation belt is relatively stable. The most important source processes for the inner belt particles were recognized to be cosmic ray albedo neutron decay (CRAND) and radial diffusion [e.g., *Walt and Farley*, 1976]. Radial diffusion has long been considered one of the most important acceleration mechanisms for radiation belt electrons, energizing electrons by bringing them inward where magnetic fields are stronger while conserving the first adiabatic invariant [e.g., *Schulz and Lanzerotti*, 1974]. As for CRAND, many studies suggest that it is an important source for energetic protons in the inner belt, but not for electrons [e.g., *Kellogg*, 1960; *Pizzella et al.*, 1962]. The loss processes for inner belt electrons include Coulomb collisions with atmospheric constituents and pitch angle scattering via wave-particle interactions with whistler mode waves. Atmospheric collisions dominate energetic electron loss only for $L < 1.3$ [*Walt*, 1964]; while above $L = 1.3$, wave-particle interaction play an important role in the loss of energetic electrons [*Abel and Thorne*, 1998]. The most important waves in the wave-particle interaction of the inner belt are plasmaspheric hiss, very low frequency (VLF) waves from high powered VLF communication transmitters, and the lightning-induced whistlers. Together with Coulomb collisions, these waves account for energetic electron loss in the inner radiation belt.

[3] The inner radiation belt is thought to be quite stable for MeV electrons and more energetic protons, but for 100s keV electrons, large variations can occur. *Pfitzer and Winckler* [1968] first reported on an inner radiation belt 100s keV electron flux enhancement during a strong geomagnetic storm in 1966 using OGO 1 and 3 satellite data. For long-term behavior, a positive correlation of the inner belt 100s keV electron fluxes at $L > 1.4$ with solar activity has been reported [*Abel et al.*, 1994]; for short-term behavior, some studies have shown that only the most intense geomagnetic storms can influence the inner belt 100s keV electron fluxes [e.g., *Bostrom et al.*, 1970]; in both cases, the flux enhancements could be attributed to enhanced inward radial diffusion from the outer radiation zone. *Sauvaud et al.* [2013], based on data from Detection of Electro-Magnetic Emissions Transmitted from Earthquake

[1]Department of Aerospace Engineering Sciences, Laboratory for Atmospheric and Space Physics, University of Colorado, Boulder, Colorado, USA.

[2]Laboratory for Space Weather, Chinese Academy of Sciences, Beijing, China.

Corresponding author: H. Zhao, Department of Aerospace Engineering Sciences, Laboratory for Atmospheric and Space Physics, University of Colorado, 3665 Discovery Dr., Boulder, CO 80303, USA. (hong.zhao@colorado.edu)

©2013. American Geophysical Union. All Rights Reserved.
2169-9380/13/10.1002/2013JA019240

Regions (DEMETER) [*Sauvaud et al.*, 2006] and found inner radiation belt electron energy structures formed by drift resonance with ULF waves measured on the ground during geomagnetic storms, which indicates enhanced radial diffusion in the inner radiation belt during storms. Also, *Selesnick* [2012] simulated inner radiation belt electron transport and compared with observations from DEMETER and found that the observed decay rates below $L = 1.5$ were much slower than predicted by scattering losses, which indicates the presence of continuous inward radial diffusion.

[4] Separating the inner and outer belt is a region called the slot region (normally $L = 2$–3, though energy dependent). The slot region is usually devoid of energetic electrons, but during strong storms, the slot region can be filled with relativistic electrons [e.g., *Blake et al.*, 1992; *Li et al.*, 1993]. The slot region is believed to form as a balance between the inward transport of electrons and pitch angle diffusion [*Lyons et al.*, 1972]. *Kim et al.* [2011] simulated the formation of the slot region using the time-dependent 3-D Versatile Electron Radiation Belt (VERB) code and indicated that the slot region forms as a balance between inward radial diffusion due to ultra low frequency (ULF) electromagnetic fluctuations and pitch angle scattering due to plasmaspheric hiss and lightning-generated whistlers. The location of the slot region depends on electron energy. For higher-energy electrons, the slot region is closer to the Earth [e.g., *Lyons and Thorne*, 1973].

[5] In this paper, we investigate 100s keV electron flux enhancements in the slot region and inner belt using electron flux data from the Instrument for the Detection of Particle (IDP) carried onboard the Detection of Electro-Magnetic Emissions Transmitted from Earthquake Regions (DEMETER) satellite, which is a microsatellite with a highly inclined low Earth orbit (710 km altitude, inclination of 98.3 degrees) [*Sauvaud et al.*, 2006]. The IDP spectrometer with a maximum geometric factor of 1.2 cm^2 sr is aimed to measure differential electron fluxes in the energy range from 70 keV to 2.5 MeV, with a time resolution of 4 s and an energy resolution of 17.8 keV in routine mode, while the measurement of higher-energy electrons (above 0.8 MeV) are not as accurate as the measurement of 70 keV–0.8 MeV electrons. Although many energetic electron flux measurements in the inner radiation belt suffer from energetic proton contamination, the energy spectrum in the inner belt from IDP data shows a series of peaks at discrete energies consistent with energetic electrons interacting with VLF waves and thus confirms the effectiveness of the IDP spectrometer in the inner radiation belt [*Sauvaud et al.*, 2006, 2008; *Selesnick et al.*, 2013].

[6] By using the IDP data, we show that 100s keV electron flux enhancements in the slot region and inner belt happen much more frequently than MeV electron flux enhancements and can occur even during moderate storms. Also, using a 1-D radial diffusion model and our diffusion coefficients, we model the flux enhancement event of April of 2010 for two different electron populations and compare the diffusion coefficients with the conventional *Kp*-dependent diffusion coefficients [*Brautigam and Albert*, 2000]. The results show that the radial diffusion coefficient in the inner belt and slot region disagree with the *Kp*-dependent diffusion coefficient, suggesting that one cannot simply extend the *Kp*-dependent diffusion coefficient to the lower L region.

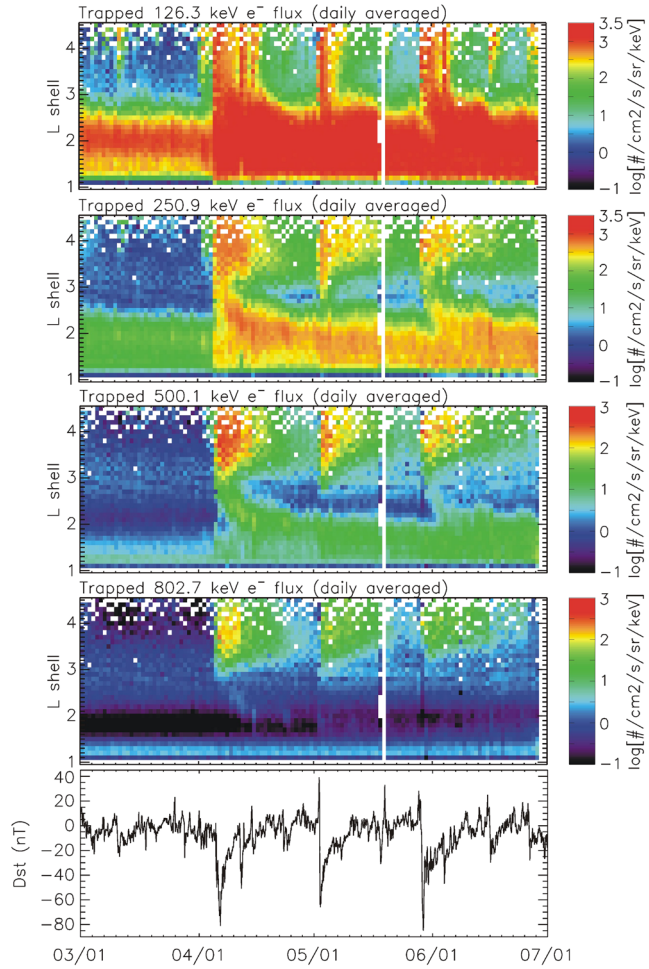

Figure 1. Daily averaged trapped energetic electron flux from different energy channels, measured by the DEMETER satellite, and the *Dst* index from 1 March 2010 to 1 July 2010.

2. Energetic Electron Flux Enhancements in the Slot Region and Inner Belt

[7] Figure 1 shows the daily averaged trapped energetic electron flux measured by DEMETER, averaged in 0.1L bins, along with the *Dst* index from March to June of 2010. Four different energy channels, 126.3 keV, 250.9 keV, 500.1 keV, and 802.7 keV, are shown (the color bars for the first two panels and the next two panels are different). It should be noted that only trapped energetic electron data are used in this paper, which means these electrons are not going to be lost during a drift period assuming no external force. We separate the measured electrons into three populations: untrapped electrons, also known as electrons in the bounce loss cone (BLC), will be lost within a bounce period; quasi-trapped electrons, or electrons in the drift loss cone (DLC), will be lost within a drift period; only the trapped electrons can survive a drift period if no scattering occurs.

[8] The regions where trapped, quasi-trapped (in DLC), and untrapped (in BLC) electron populations were measured from 1 to 10 March 2010 by DEMETER are shown in Figure 2. The calculation for the different electron populations was based on the DEMETER orbital information, local

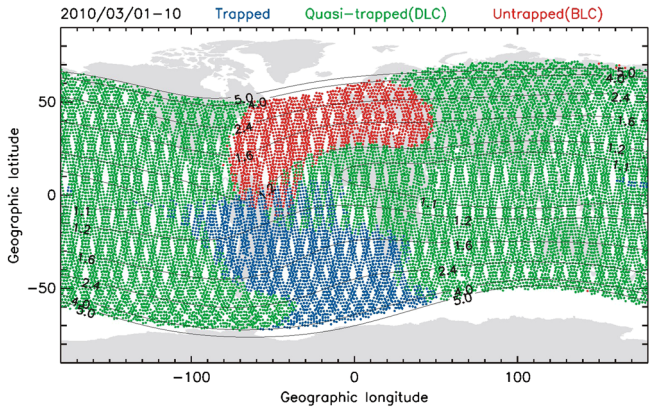

Figure 2. Trapped/quasi-trapped (DLC)/untrapped (BLC) electron populations measured by DEMETER IDP, shown in blue, green, and red, respectively, from 1 to 10 March 2010. The calculation was based on the DEMETER orbital information, local pitch angle of the detector axis, and the IGRF model. The electron is assumed to be lost when it reaches 100 km altitude.

pitch angle of the detector axis, and the IGRF model. We assume that the electron will be lost when it reaches 100 km altitude. In this paper, we focus on the trapped electron population, which is mainly measured near the South Atlantic Anomaly (SAA) and is shown as the blue region in Figure 2.

[9] It is evident in Figure 1 that from March to June 2010, there are several energetic electron penetrations into the slot region and inner belt. At the beginning of April, the strongest penetration during these 4 months occurred, which filled the whole slot region and strongly enhanced the energetic electron flux in the inner belt, particularly for the lower-energy electrons. The flux enhancement during this April event occurred as low as $L \sim 1.2$. For 126.3 keV electrons, this penetration into the inner belt happened almost immediately (based on finer resolution data which are not shown here, the flux doubled at $L = 2$ within half a day), while 250.9 keV and 500.1 keV electrons slowly diffuse inward to the inner belt. Even for the highest energy channel of IDP used in this study, 802.7 keV electrons, we can also see the filling of the slot region after the April event. It is also evident that the deep penetrations happened during geomagnetic storms. However, these storms are just moderate, with –100 nT < minimum *Dst* < –50 nT. This shows that although MeV electron injections into the slot region mostly occur during strong storms and intense solar wind conditions [e.g., *Baker et al.*, 2007; *Zhao and Li*, 2013], for 100s keV electrons, flux enhancements in the slot region and inner belt occur much more often.

[10] In the next section, we transform the flux into the phase space density (PSD), then model the April flux enhancement event using a 1-D radial diffusion model.

3. Modeling Energetic Electron Penetration Into the Slot Region and Inner Belt

3.1. Phase Space Density (PSD) Calculation

[11] In order to model the flux enhancement event during April 2010 using a radial diffusion model, we need to transform the flux data into PSD. First, we need to determine the corresponding phase space coordinates, μ, K and L^*, based on the satellite position, electron energy, and the local pitch angle information. The first adiabatic invariant, μ, can be calculated using the following:

$$\mu = \frac{P_\perp^2}{2m_0 B} \tag{1}$$

where $P_\perp$ is the relativistic momentum component perpendicular to the local magnetic vector, m_0 is the rest mass of electron, and B is the local magnetic field magnitude. The second adiabatic invariant, K, can be calculated as follows:

$$K = \int_{S_m}^{S_m'} \sqrt{B_m - B(S)}\, \mathrm{d}s \tag{2}$$

where S_m and S_m' are two mirror points, B_m and $B(S)$ are the magnetic field strength of mirror points and position S, respectively, and ds is the distance along the magnetic field line. The Roederer L, L^*, is defined as the radial distance in Earth radii to the equatorial point of the shell on which the electron would be found, if all nondipolar perturbations of the magnetic field are adiabatically turned off [*Roederer*, 1970]. It can be calculated as follows:

$$L^* = \frac{2\pi M}{|\Phi| R_E} \tag{3}$$

where M is the Earth's dipole magnetic moment, R_E is the Earth's radius, and Φ is the third adiabatic invariant, which is the magnetic flux enclosed by the electron drift shell and can be calculated by

$$\Phi = \int_S \vec{B} \cdot \vec{\mathrm{d}S} \tag{4}$$

where B is the magnetic vector and S is the cross section of the drift shell.

[12] Based on these equations, we can calculate μ, K, and L^* for each data point. In this paper, we use the IRBEM library [*Boscher et al.*, 2010] to do the magnetic field-related calculations and use *LANL** [*Yu et al.*, 2012] to calculate L^*. In our calculation, we use T89 as the external magnetic field model [*Tsyganenko*, 1989]. Based on the calculation, however, we found that according to DEMETER's measurements, we can only derive a very limited L^* range for the electrons with the same μ and K. This is mainly caused by the limited pitch angle coverage that DEMETER can provide due to its low Earth orbit.

[13] In order to investigate the radial transport of the electrons, we need to examine a relatively large L^* range for electrons with the same first and second adiabatic invariants. Thus, we have to make some assumptions about the pitch angle distribution. *Gannon et al.* [2007] have investigated the pitch angle distribution of energetic electrons using data from the Combined Release and Radiation Effects Satellite (CRRES). They showed that 90°-peaked distributions dominate at 100s keV energies, especially at lower L shells near the equator. By fitting the pitch angle distribution with a $\sin^n \alpha$ form, where α is the local pitch angle, they found that n mainly varies between 2 and 5, between $L = 3$ and 8, and that 90°-peaked distributions are typically steeper at lower L. In this study, we assume a $\sin^3 \alpha$ pitch angle distribution. A discussion of the influence of the pitch angle distribution assumption on the model results will be presented in the next section.

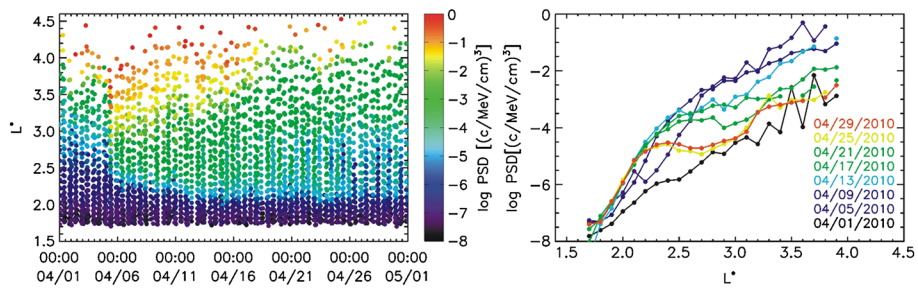

Figure 3. (left) PSD data for μ = 30 MeV/G equatorially trapped electrons, assuming the pitch angle distribution at the equator has $\sin^3 \alpha$ form. (right) Daily averaged radial profile of PSD for μ = 30 MeV/G equatorially trapped electrons during April 2010.

[14] With this pitch angle distribution assumption, we can focus on equatorially trapped electrons (K = 0). First, for each data point, we trace the field line to the magnetic equator and calculate the equatorial pitch angle; then, based on the $\sin^3 \alpha$ pitch angle distribution assumption and the measured flux data, we calculate the flux and μ for 90° equatorial pitch angle electrons. Then we can derive L^* for each data point using *LANL**. Finally, we calculate the PSD according to the equation used in *Chen et al.* [2005]:

$$f = \left[\frac{j}{p^2c^2} * 1.66 \times 10^{-10}\right] \times 200.3 \tag{5}$$

where j is the flux in units of cm^{-2} s^{-1} sr^{-1} keV^{-1}, p is the relativistic momentum, c is the speed of light, and f is the PSD. The multiplying factor here is used to transform the PSD to the GEM (Geospace Environment Modeling) units (c/MeV/cm)^3.

[15] In this study, we model two different equatorially trapped electron populations: μ = 28.5–31.5 MeV/G (denoted as μ = 30 MeV/G) and μ = 14.25–15.75 MeV/G (denoted as μ = 15 MeV/G). Electrons with μ = 30 MeV/G correspond to equatorially trapped electrons with an energy of 250 keV at $L^* \sim 3$ or 500 keV at $L^* \sim 2.2$, while the electrons with μ = 15 MeV/G corresponds to equatorially trapped electrons with an energy of 250 keV at $L^* \sim 2.4$ or 500 keV at $L^* \sim 1.8$. Figure 3 (left) shows the PSD for electrons with μ = 30 MeV/G, and Figure 3 (right) shows the daily averaged PSD radial profile during April 2010, while Figure 4 shows similar figures for μ = 15 MeV/G electrons.

[16] As Figure 3 shows, the PSD for μ = 30 MeV/G equatorially trapped electrons enhanced significantly throughout the slot region and the enhancement happened as low as $L^* \sim 2$. For μ = 15 MeV/G equatorially trapped electrons, the PSD enhancement happened even lower, reaching $L^* \sim 1.8$. From the radial profile, we find that for μ = 30 MeV electrons, the enhancement happened in the outer region first and then slowly diffused inward to the slot region and inner belt. For μ = 15 MeV electrons, however, the PSD enhancement in the inner belt occurs faster. After the deep penetration, μ = 30 MeV electrons slowly decayed and formed a slot-like radial profile at the end of April, while for μ = 15 MeV electrons this feature is not so clear.

3.2. Model Description

[17] The radial diffusion model in this paper uses the Fokker-Planck equation [*Schulz and Lanzerotti*, 1974]:

$$\frac{\partial f}{\partial t} = L^{*2}\frac{\partial}{\partial L^*}\left(\frac{D_{LL}}{L^{*2}}\frac{\partial f}{\partial L^*}\right) - \frac{f}{\tau} \tag{6}$$

where $f(L^*, t)$ is the drift period-averaged phase space density for fixed μ and K, D_{LL} is the radial diffusion coefficient, and τ is the electron lifetime. This equation can be solved numerically.

[18] The radial diffusion coefficient, D_{LL}, is set as

$$D_{LL} = D_0\left(\frac{L^*}{L_{\max}}\right)^4 \tag{7}$$

where $L_{\max}$ is the L^* of the outer boundary used in our model. The temporal part of D_{LL} used in this paper is similar to the one used in *Li et al.* [2009]:

$$D_0 = c\left(\frac{v}{v_0}\right)^{\gamma_1}[1 + (v_x B_z + |v_x B_z|)/\alpha]^{\gamma_2} \tag{8}$$

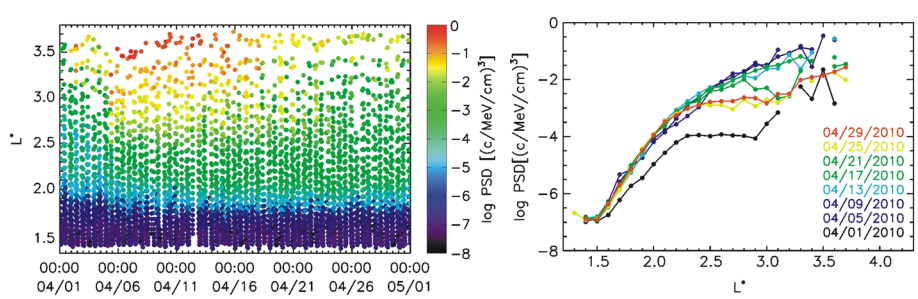

Figure 4. (left) PSD data for μ = 15 MeV/G equatorially trapped electrons, assuming the pitch angle distribution at the equator has $\sin^3 \alpha$ form. (right) Daily averaged radial profile of PSD for μ = 15 MeV/G equatorially trapped electrons during April 2010.

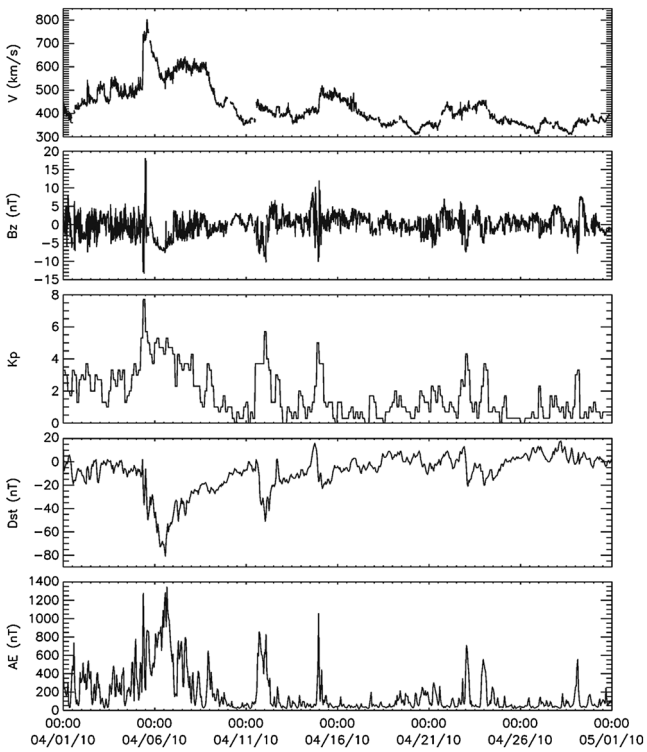

Figure 5. Solar wind speed, IMF B_z in GSM coordinates, *Kp*, *Dst*, and *AE* indices during April 2010.

where c, α, γ_1, and γ_2 are constants, v is the solar wind speed, v_0(= 404 km/s) is the average solar wind speed in 2010, v_x and B_z are the x component of solar wind speed and z component of interplanetary magnetic field (IMF), respectively. The γ parameters determine the relative contribution of the solar wind speed and the convection electric field. The solar wind speed term represents the energy transfer from dayside compression and through the Kelvin-Helmholtz instability; the convection electric field term represents the energy transfer from dayside reconnection. The solar wind speed, IMF B_z, and geomagnetic indices during April 2010 are shown in Figure 5. It can be seen that around 5 April, which corresponds to the time of deep electron penetration, there is an impulse in the solar wind speed and IMF B_z, with *Kp* of $\sim$ 8 and elevated *AE* index. The minimum *Dst* index during the first several days in April is about –80 nT, indicating a moderate geomagnetic storm.

[19] The electron lifetime, τ, used in this paper has no temporal variation, but has a spatial variation. Because of the presence of the slot region, we calculate the lifetime in two regions separately, divided by $L_{\rm cri}$ (to be discussed later). In each region, the lifetime is set as

$$\tau = \tau_0 \left(\frac{L_{\max}}{L^*}\right)^p \tag{9}$$

where τ_0 and p are constants, and $L_{\max}$ is the L^* of the outer boundary used in the model.

[20] So far we have nine parameters in the radial diffusion model: c, α, γ_1, γ_2, τ_{01}, τ_{02}, p_1, p_2, and $L_{\rm cri}$, which need to be optimized by fitting the PSD data. Here for τ_0 and p suffix 1 denotes the region outside $L_{\rm cri}$, and suffix 2 refers to the region inside $L_{\rm cri}$.

[21] Based on the PSD data, we choose $L^* = 4$ and $L^* = 1.8$ as the outer and inner boundary for modeling $\mu = 30$ MeV electron PSD evolution, and $L^* = 3.5$ and $L^* = 1.5$ for $\mu = 15$ MeV electrons. The outer and inner boundary data are averaged over $0.2L$ with a time resolution of 10 min, and then interpolated across data gaps. The initial condition is set to be the PSD data averaged over 2 h and interpolated across L^*. To compare with the model results, the PSD data are also averaged in the model frame, which has a time resolution of 10 min and has been divided into 500 bins in L^* between outer and inner boundaries. In order to optimize the model results, we choose to minimize the root-mean-square deviation (RMSD), which is defined as

$$\text{RMSD} = \sqrt{\frac{\sum_1^n \left(\log\left(\frac{f}{\hat{f}}\right)\right)^2}{n}} \tag{10}$$

where $\hat{f}$ is the PSD calculated by the radial diffusion model, f is the PSD data, and n is the number of the data points. The optimized model results are shown in the next subsection.

3.3. Model Results

[22] Since we focus on the slot region and inner belt, we optimize the model results for $\mu = 30$ MeV/G electrons by minimizing the RMSD between $L^* = 2.0$ and $L^* = 3.0$. The optimized parameters are $c = 0.0104$, $\gamma_1 = 2.8$, $\gamma_2 = 0.85$, $\alpha = 1652$ km nT/s, $L_{\rm cri} = 3.27$, $\tau_{01} = 3.40$, $p_1 = -2.91$, $\tau_{02} = 0.81$, and $p_2 = 4.21$. Figure 6 shows the phase space density data and the optimized model results for $\mu = 30$ MeV/G electrons. Figure 7 shows the model results at various L^* compared with the original PSD data. We also calculated the prediction efficiency (PE) and linear correlation coefficient (LC) at different L^* inside the slot region and inner belt. The PE is defined as follows:

$$PE = 1 - \frac{\sum_i^n (\log f_i - \log \hat{f}_i)^2}{\sum_i^n (\log f_i - \overline{\log f})^2} \tag{11}$$

where f and $\hat{f}$ are the PSD data and the PSD calculated by the radial diffusion model, respectively, $\overline{\log f}$ is the mean of the logarithm of PSD data, which in this paper is the averaged $\log f$ at a specific L^* over a month, and n is the number of data points. The *PE* shows the agreement between the model results and the corresponding data: $PE = 0$ indicates the model results are as good as the averaged data; $PE > 0$ shows that the model is better than taking the average, and $PE = 1$ means a perfect modeling.

[23] As can be seen in Figure 6, the model results reproduce well the main features in the PSD data, especially in the slot region and inner belt. The model results perfectly reproduce the deep penetration around 5 April; after that, the model results also show that electrons slowly diffuse inward; at the end of April, the model predicts the reappearance of the slot region, which agrees with the PSD data.

[24] Figure 7 shows that in the slot region ($L^* = 2$–3), the model results fit the data quite well too. At $L^* = 2.9 \pm 0.1$, 2.6 ± 0.1, 2.3 ± 0.1, and 2.0 ± 0.1, the PEs are 0.79, 0.84, 0.60, and 0.51, respectively, and the LCs are 0.92, 0.92, 0.84, and 0.74, respectively, showing that the model results in the slot region reproduce the data with high accuracy. The PE at $L^* = 2.0$ is relatively low, which is mainly caused by the low variation of the PSD data at $L^* = 2.0$.

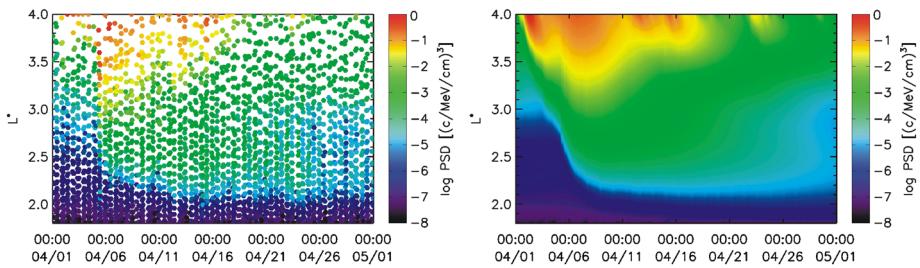

Figure 6. (left) Phase space density data and the (right) radial diffusion model results for μ = 30 MeV/G equatorially trapped electrons.

[25] For μ = 15 MeV/G electrons, we optimize the model results by minimizing the RMSD between L^* = 1.8 and L^* = 3.0, since for μ = 15 MeV/G the deep penetration can reach as low as L^* = 1.8. The parameters used in the model are c = 0.000345, γ_1 = 5.1, γ_2 = 2.1, α = 1208 km nT/s, $L_{\rm cri}$ = 2.67, τ_{01} = 3.80, p_1 = 1.69, τ_{02} = 0.60, and p_2 = 8.50. The optimized model results are shown in Figures 8 and 9.

[26] As shown in Figures 8 and 9, the model results reproduce the PSD data quite well throughout the slot region and inner belt. The penetration of μ = 15 MeV/G electrons occurred much faster, which is reproduced by the model; while after the initial injection, model results show that the inward radial diffusion is not very efficient, and the electrons decay quite slowly below $L^* \sim 2.5$, which is also consistent with the original PSD data. The PEs for different L^* in the slot region and inner belt are up to 0.82, and the LCs can be as high as 0.91.

[27] It is also worth mentioning that we also tried to substitute the inner boundary condition here with commonly used condition PSD = 0. Since the inner boundary PSDs are quite small, setting PSD = 0 at the inner boundary almost does not influence the model results. For example, for μ = 30 MeV/G electrons, by setting PSD = 0 at L^* = 1.8 and using the same parameters, PEs at $L^* = 2.9 \pm 0.1, 2.6 \pm 0.1, 2.3 \pm 0.1$ and 2.0 ± 0.1 are 0.79, 0.84, 0.60 and 0.50, respectively, which are almost the same with the results using PSD data at the inner boundary.

4. Discussion

4.1. The Radial Diffusion Coefficient

[28] The diffusion coefficients D_{LL} used in the radial diffusion model for μ = 30 MeV/G electrons and μ = 15 MeV/G electrons at different L^* are shown in Figure 10, along with the Kp-dependent diffusion coefficients from *Brautigam and Albert* [2000]. The Kp-dependent D_{LL} includes electrostatic (D_{LL}^E) and electromagnetic (D_{LL}^B) contributions. The electrostatic radial diffusion coefficient used by *Brautigam and Albert* [2000] is given by

$$D_{LL}^E = \frac{1}{4}\left(\frac{cE_{\rm rms}}{R_E B_0}\right)^2 \left[\frac{T}{1+(\omega_D T/2)^2}\right] L^6 \tag{12}$$

$$\omega_D = \left(\frac{3\mu c}{eL^2 R_E^2}\right)\left(1+\frac{2\mu B}{E_0}\right)^{-1/2} \tag{13}$$

where ω_D is the electron drift frequency, $E_{\rm rms}$ is the root mean square of the electric field amplitude and is assumed as $E_{\rm rms}(Kp) = 0.26(Kp-1)+0.1$ mV/m, Kp = 1 to 6, T is the exponential decay time (0.75 h), B_0 is the dipole moment,

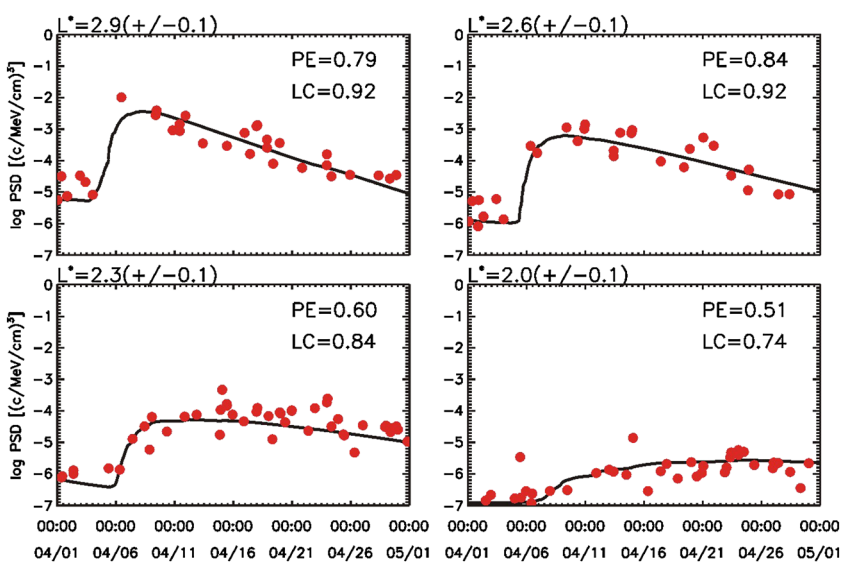

Figure 7. Comparison of model results and the original PSD data (at different L^*) for μ = 30 MeV/G equatorially trapped electrons. The prediction efficiency (PE) and linear correlation coefficient (LC) for each panel are shown in the figure.

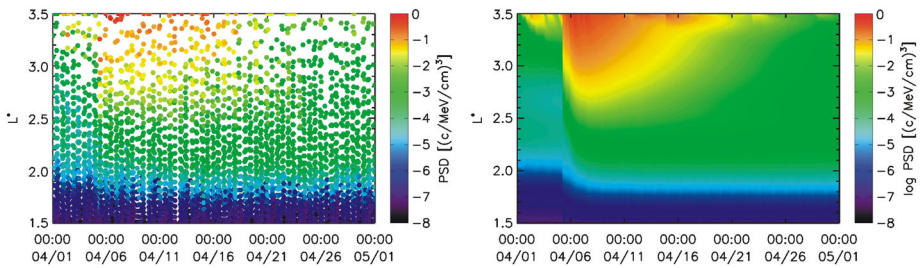

Figure 8. (left) Phase space density data and the (right) radial diffusion model results for μ = 15 MeV/G equatorially trapped electrons.

and E_0 is the electron rest energy. It can be seen from the equation that D_{LL}^{E} is dependent on μ. The electromagnetic diffusion coefficient used by *Brautigam and Albert* [2000] is $D_{LL}^{Kp} = 10^{0.506Kp-9.325}L^{10}$, Kp = 1 to 6, and has no dependence on μ. These equations were originally used for L = 3–6.6. However, here we simply extend it to the slot region and inner belt. The D_{LL}s of our model shown in Figure 10 are averaged over 1 h.

[29] Comparing the diffusion coefficient of the two different electron populations used in this paper, D_{LL} for μ = 15 MeV/G electrons is larger than D_{LL} for μ = 30 MeV/G electrons at the time of deep penetration, but is lower than that after the penetration, which is consistent with the fact that lower-energy electrons are transported inward much faster, while higher-energy electrons slowly diffuse inward. The radial diffusion coefficients depend on power spectrum of electric and magnetic field fluctuations, for which the information is not available for this study. However, there should not be such a large difference in radial diffusion coefficients in general between μ = 15 MeV/G and μ = 30 MeV/G electrons only at the time of deep penetration. So there can be some other nonadiabatic processes involved at that time, the effects of which seem to be well represented by our empirical radial diffusion model, and thus the large diffusion coefficient of μ = 15 MeV/G electrons at the time of penetration might not represent the real radial diffusion coefficient in a physical sense.

[30] It is widely believed that the magnetic diffusion coefficient is substantially larger than the electric diffusion coefficient in the outer radiation belt. Recently, based on global MHD simulations and satellite measurements, *Tu et al.* [2012] have discussed the complexity of the radial diffusion coefficient and found that inside L = 4, the contribution to the diffusion coefficient mainly comes from electric field fluctuations rather than magnetic field perturbations; also, *Ozeke et al.* [2012] calculated the electromagnetic and electrostatic diffusion coefficients using ground- and space-based observations of ULF wave power and found that electric field diffusion is much more important than magnetic field diffusion between L = 3 and 7. By extending the Kp-dependent diffusion coefficients from *Brautigam and Albert* [2000] to the slot region and inner belt, as shown in Figure 10, it is apparent that at low L shells, their electrostatic diffusion coefficient is much larger than the electromagnetic one, indicating that radial diffusion is most likely caused by electric field perturbations rather than magnetic field perturbations. Comparing the diffusion coefficients used in this paper with the Kp-dependent ones, we

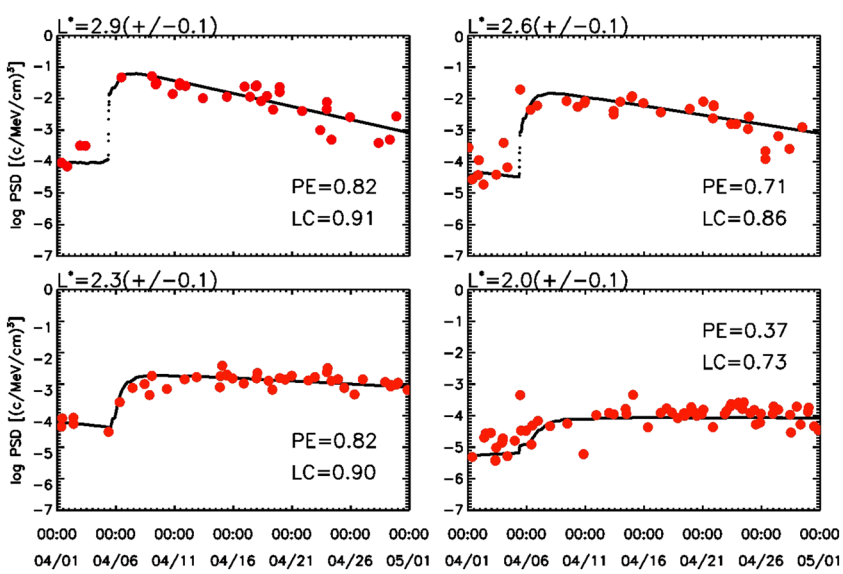

Figure 9. Comparison of model results and the original PSD data (at different L^*) for μ = 15 MeV/G equatorially trapped electrons. The prediction efficiency (PE) and linear correlation coefficient (LC) for each panel are shown in the figure.

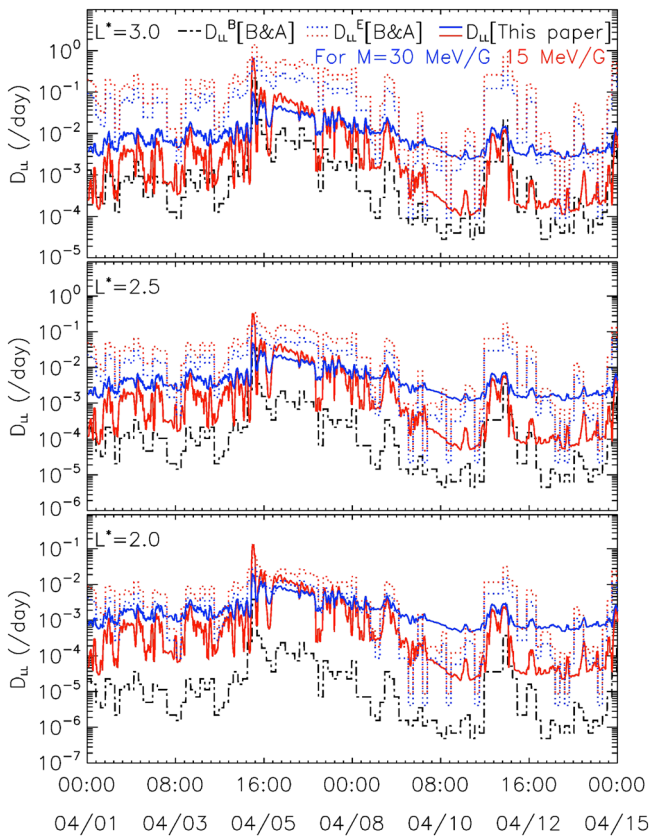

Figure 10. Diffusion coefficient D_{LL} for μ = 30 MeV/G, K = 0 electrons and μ = 15 MeV/G, K = 0 electrons at different L^*, along with the *Kp*-dependent diffusion coefficients from *Brautigam and Albert* [2000] during 1–15 April 2010.

show that in the slot region and inner belt, the diffusion coefficients in our model are much higher than the widely used *Kp*-dependent electromagnetic diffusion coefficient D^B_{LL}, and the difference gets larger as L^* becomes smaller. However, the diffusion coefficients used in this paper are smaller than the *Kp*-dependent electrostatic diffusion coefficient D^E_{LL}, especially at larger L^*, and the difference gets smaller as L^* gets smaller. Also, comparing the diffusion coefficients for different μ, it is apparent that our results show more dynamic features than *Kp*-dependent ones, especially for lower μ electrons. Our results indicate that radial diffusion coefficients for different μ have different dependence on solar wind parameters, and rather than a constant scaling factor as used by *Brautigam and Albert* [2000], the difference between diffusion coefficients for different μ changes in time. This indicates that the *Kp*-dependent diffusion coefficient cannot be simply extended into the lower L region and applied to different μ electrons.

[31] The disagreement between $D_{LL}(Kp)$ and D_{LL} used in this paper in the slot region and inner belt also suggests a different L dependence, rather than L^{10} or L^6, for the radial diffusion coefficient. To reproduce the data, we used a lower power in order to increase the diffusion coefficient at lower L shells and maintain a reasonable value of the diffusion coefficient in the outer belt. By trying with several different integers, the best result we found is a dependence of L^4. We also tried higher L powers, for example, a dependence of L^6 for μ = 30 MeV/G electrons, and tuned the parameters by optimizing the results in the slot region. The optimized results were similar to the one derived using a dependence of L^4 in the lower L region, with the PEs at $L^* = 2.9 \pm 0.1, 2.6 \pm 0.1, 2.3 \pm 0.1$, and 2.0 ± 0.1 are 0.75, 0.75, 0.47, and 0.58, respectively. However, once the parameters are tuned for optimizing the result between L^* = 2 and 3, the results at $L^* > 3$ do not fit the data as well as the results using L^4 dependence. For example, at L^* = 3.4, using a dependence of L^6, the PE is negative; while a dependence of L^4 gives a PE of 0.44.

[32] On the other hand, there are always some trade-off between the radial diffusion coefficient and electron lifetime. So we also examine the sensitivity of our model to D_{LL} and τ. In our model, by increasing D_{LL} and decreasing τ, we can get somewhat similar results within the slot region and inner belt; however, the results in the outer part ($L^* > 3$) do not fit the data well. For example, for μ = 30 MeV/G electrons, we increased D_{LL} by 50% and tuned the parameters τ_{01}, τ_{02}, p_1, p_2, and $L_{\rm cri}$ to minimize the RMSD between L^* = 2.0 and L^* = 3.0. As a result, PEs at $L^* = 2.9 \pm 0.1, 2.6 \pm 0.1, 2.3 \pm 0.1$, and 2.0 ± 0.1 are 0.79, 0.84, 0.56, and 0.26, respectively; while at L = 3.4, PE is –1.68, showing bad agreement between the model and data. However, our model is based on the assumption that τ is constant in time. Considering the time-varying τ, we might get similar results by increasing D_{LL} and decreasing τ or opposite.

4.2. The Electron Lifetime

[33] Figure 11 shows the electron lifetime used in the diffusion model for μ = 30 MeV/G electrons (Figure 11, left) and μ = 15 MeV/G electrons (Figure 11, right), versus L^* and the approximate corresponding electron energy. For μ = 30 MeV/G electrons, the decay time is about 3 days at L^* = 3 (corresponding to ~250 keV electrons) and about 10 days at L^* = 2.2 (~500 keV electrons); for μ = 15 MeV/G electrons, the decay time is about 10 days

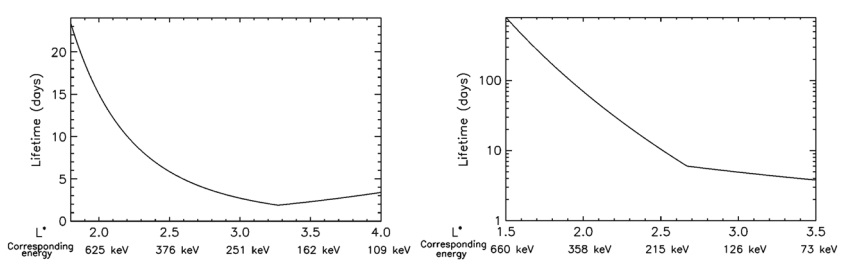

Figure 11. Electron lifetime used in the model for (left) μ = 30 MeV/G equatorially trapped electrons and (right) μ = 15 MeV/G equatorially trapped electrons, versus L^* and corresponding electron energy.

at $L^* = 2.4$ (~250 keV electrons) and about 170 days at $L^* = 1.8$ (~500 keV electrons). It is well accepted that in the outer radiation belt, 100s keV and higher-energy electron lifetime is expected to increase with increasing energy at a fixed L. However, since the electron lifetime depends on the loss processes, the situation is quite different for the slot region and inner belt. Comparing the electron lifetime for $\mu = 30$ MeV/G and $\mu = 15$ MeV/G in the lower L region, e.g., at $L^* = 2.0$, the lifetime for higher-energy electrons (625 keV for $\mu = 30$ MeV/G electrons) is much lower than lower-energy electrons (358 keV for $\mu = 15$ MeV/G). The decreasing electron lifetimes with increasing electron energy in the slot region and inner belt is a result of wave-particle interaction. Although the relative importance of plasmaspheric hiss, VLF waves from transmitters, and the lightning-induced whistlers is still debatable, this result shows that in the slot region and inner belt, for 100s keV electrons, the resonant interaction with electromagnetic waves is more significant for higher-energy electrons. *Lyons et al.* [1972] calculated the theoretical precipitation lifetimes for different energy electrons inside the plasmapause due to plasmaspheric whistler mode wave scattering, and showed that at lower L, the electron lifetime decreases with increasing energy, which is consistent with our results. This feature is also consistent with the fact that the slot region is closer to the Earth for higher-energy electrons and the inner belt extends further for lower-energy electrons.

[34] In the model, we calculated τ in two regions, divided by L_{cri}. It is evident that the electron lifetime used in the model for $\mu = 30$ MeV/G electrons has a minimum at $L_{\mathrm{cri}} = 3.27$, which accounts for the reappearance of the slot region. The slot region forms as a balance between inward radial diffusion and scattering. Below $L_{\mathrm{cri}} = 3.27$, closer to the Earth, the lifetime gets longer and the diffusion rate gets lower too, thus the balance between the two forms a slot region centered around $L^* = 2.9$, as shown in Figure 6. For $\mu = 15$ MeV/G electrons, there is no clear feature of a slot region, and the two-region lifetime is used to give a better fit to the original PSD data.

4.3. The Pitch Angle Assumption

[35] All PSD data we used are derived based on the assumption that the pitch angle distribution at the magnetic equator has the form of $\sin^3\alpha$. To check the sensitivity of this assumption, we also tried to use $\sin^2\alpha$ and $\sin^5\alpha$ as the pitch angle distribution assumption. The results show that, although the magnitude of PSD data changes a lot, the shape of PSD profile does not change much, and thus the diffusion coefficients used in the model are very similar. The distribution of $\sin^2\alpha$ gives a $\sim$ 20% higher radial diffusion coefficient than $\sin^3\alpha$, while the distribution of $\sin^5\alpha$ gives a $\sim$ 30% lower diffusion coefficient. Thus, the uncertainties in pitch angle distribution assumption do not significantly affect the result that the diffusion coefficient needed in this April event disagrees with the *Kp*-dependent diffusion coefficients from *Brautigam and Albert* [2000] in the slot region and inner belt.

[36] While uncertainties about diffusion coefficients and lifetimes used here exist, we demonstrate that fast enhancements of energetic electrons in the slot region and inner belt can be understood as the inward radial transport of lower-energy electrons originally at larger L.

5. Conclusion

[37] We investigated 100s keV electron flux enhancements in the slot region and the inner belt using DEMETER IDP data, and modeled the flux enhancement event of April 2010 for $\mu = 30$ MeV/G and $\mu = 15$ MeV/G equatorially trapped electrons. The results are summarized as follows:

[38] 1. For 100s keV electrons, the flux enhancements in the slot region and inner belt occur much more often than MeV electrons. Even moderate geomagnetic storms can cause 100 keV electron flux enhancement in the lower L region.

[39] 2. By using a 1-D radial diffusion model, we modeled the radial diffusion of $\mu = 30$ MeV/G and $\mu = 15$ MeV/G equatorially trapped electrons in April 2010. The model results reproduce the PSD data calculated from the electron flux data quite well, indicating that the flux enhancement event can be well explained by inward radial transport.

[40] 3. Comparing the diffusion coefficients used in our model with the *Kp*-dependent diffusion coefficient $D_{LL}(Kp)$ from *Brautigam and Albert* [2000], we found that our diffusion coefficients are much larger than D_{LL}^B but smaller than D_{LL}^E, showing that the widely used $D_{LL}(Kp)$ cannot be simply extended into the slot region and inner belt.

[41] **Acknowledgments.** The authors are indebted to Richard Selesnick for his support for this work, including his suggestion to illustrate three populations of energetic electrons measured by a highly inclined and low Earth orbit satellite. We acknowledge the helpful comments and suggestion from Michael Temerin and the careful proofreading by Lauren Blum. We also would like to thank Lauren Blum, Quintin Schiller, Allison Jaynes, and Sam Califf for insightful discussions. The authors thank J.-A. Sauvaud for providing access to the DEMETER/IDP data and for advice on their interpretation. This work is supported by NASA grants (NNX-10AQ48G, and -09AF47G) and NSF grant (ATM-0842388), and also by grant from the National Natural Science Foundation of China (41231067).

[42] Masaki Fujimoto thanks the reviewers for their assistance in evaluating this paper.

References

Abel, B., R. M. Thorne, and A. L. Vampola (1994), Solar cyclic behavior of trapped energetic electrons in Earth's inner radiation belt, *J. Geophys. Res.*, *99*(A10), 19,427–19,431.

Abel, B., and R. M. Thorne (1998), Electron scattering loss in Earth's inner magnetosphere: 1. Dominant physical processes, *J. Geophys. Res.*, *103*(A2), 2385–2396.

Baker, D. N., S. G. Kanekal, R. B. Home, N. P. Meredith, and S. A. Glauert (2007), Low-altitude measurements of 2–6 MeV electron trapping lifetimes at $1.5 \leq L \leq 2.5$, *Geophys. Res. Lett.*, *34*, L20110, doi:10.1029/2007GL031007.

Blake, J. B., W. A. Kolasinski, R. W. Fillius, and E. G. Mullen (1992), Injection of electrons and protons with energies of tens of MeV into L < 3 on 24 March 1991, *Geophys. Res. Lett.*, *19*(8), 821–824.

Boscher, D., S. Bourdarie, P. O'Brien, and T. Guild (2010), IRBEM library V4.3, 2004–2008, ONERA-DESP, Toulouse France, Aerospace Corporation, Washington, D. C.

Bostrom, C. O., D. S. Beall, and J. C. Armstrong (1970), Time history of the inner radiation zone, October 1963 to December 1968, *J. Geophys. Res.*, *75*(7), 1246–1256.

Brautigam, D. H., and J. M. Albert (2000), Radial diffusion analysis of outer radiation belt electrons during the October 9, 1990, magnetic storm, *J. Geophys. Res.*, *105*(A1), 291–309, doi:10.1029/1999JA900344.

Chen, Y., R. H. W. Friedel, G. D. Reeves, T. G. Onsager, and M. F. Thomsen (2005), Multisatellite determination of the relativistic electron phase space density at geosynchronous orbit: Methodology and results during geomagnetically quiet times, *J. Geophys. Res.*, *110*, A10210, doi:10.1029/2004JA010895.

Gannon, J. L., X. Li, and D. Heynderickx (2007), Pitch angle distribution analysis of radiation belt electrons based on Combined Release and Radiation Effects Satellite Medium Electrons A data, *J. Geophys. Res.*, *112*, A05212, doi:10.1029/2005JA011565.

Kellogg, P. J. (1960), Electrons of the Van Allen radiation, *J. Geophys. Res.*, *65*(9), 2705–2713.

Kim, K.-C., Y. Shprits, D. Subbotin, and B. Ni (2011), Understanding the dynamic evolution of the relativistic electron slot region including radial and pitch angle diffusion, *J. Geophys. Res.*, *116*, A10214, doi:10.1029/2011JA016684.

Li, X., I. Roth, M. Temerin, J. Wygant, M. K. Hudson, and J. B. Blake (1993), Simulation of the prompt energization and transport of radiation belt particles during the March 24, 1991 SSC, *Geophys. Res. Lett.*, *20*, 2423–2426.

Li, X., A. B. Barker, D. N. Baker, W. C. Tu, T. E. Sarris, R. S. Selesnick, R. Friedel, and C. Shen (2009), Modeling the deep penetration of outer belt electrons during the "Halloween" magnetic storm in 2003, *Space Weather*, *7*, S02004, doi:10.1029/2008SW000418.

Lyons, L. R., R. M. Thorne, and C. F. Kennel (1972), Pitch-angle diffusion of radiation belt electrons within the plasmasphere, *J. Geophys. Res.*, *77*(19), 3455–3474.

Lyons, L. R., and R. M. Thorne (1973), Equilibrium structure of radiation belt electrons, *J. Geophys. Res.*, *78*(13), 2142–2149.

Ozeke, L. G., I. R. Mann, K. R. Murphy, I. J. Rae, D. K. Milling, S. R. Elkington, A. A. Chan, and H. J. Singer (2012), ULF wave derived radiation belt radial diffusion coefficients, *J. Geophys. Res.*, *117*, A04222, doi:10.1029/2011JA017463.

Pfitzer, K. A., and J. R. Winckler (1968), Experimental observation of a large addition to the electron inner radiation belt after a solar flare event, *J. Geophys. Res.*, *73*(17), 5792–5797.

Pizzella, G., C. D. Laughlin, and B. J. O'Brien (1962), Note on the electron energy spectrum in the inner Van Allen belt, *J. Geophys. Res.*, *67*(9), 3281–3287.

Roederer, J. G. (1970), *Dynamics of Geomagnetically Trapped Radiation*, Springer-Verlag, New York.

Sauvaud, J. A., T. Moreau, R. Maggiolo, J.-P. Treilhou, C. Jacquey, A. Cros, J. Coutelier, J. Rouzaud, E. Penou, and M. Gangloff (2006), High-energy electron detection onboard DEMETER: The IDP spectrometer, description and first results on the inner belt, *Planet. Space Sci.*, *54*, 502–511.

Sauvaud, J.-A., R. Maggiolo, C. Jacquey, M. Parrot, J.-J. Berthelier, R. J. Gamble, and C. J. Rodger (2008), Radiation belt electron precipitation due to VLF transmitters: Satellite observations, *Geophys. Res. Lett.*, *35*, L09101, doi:10.1029/2008GL033194.

Sauvaud, J.-A., M. Walt, D. Delcourt, C. Benoist, E. Penou, Y. Chen, and C. T. Russell (2013), Inner radiation belt particle acceleration and energy structuring by drift resonance with ULF waves during geomagnetic storms, *J. Geophys. Res. Space Physics*, *118*, 1723–1736, doi:10.1002/jgra.50125.

Schulz, M., and L. Lanzerotti (1974), *Particle Diffusion in the Radiation Belts*, Springer, New York.

Selesnick, R. S. (2012), Atmospheric scattering and decay of inner radiation belt electrons, *J. Geophys. Res.*, *117*, A08218, doi:10.1029/2012JA017793.

Selesnick, R. S., J. M. Albert, and M. J. Starks (2013), Influence of a ground-based VLF radio transmitter on the inner electron radiation belt, *J. Geophys. Res. Space Physics*, *118*, 628–635, doi:10.1002/jgra.50095.

Tsyganenko, N. A. (1989), A magnetospheric magnetic field model with a warped tail current sheet, *Planet. Space Sci.*, *37*, 5–20.

Tu, W., S. R. Elkington, X. Li, W. Liu, and J. Bonnell (2012), Quantifying radial diffusion coefficients of radiation belt electrons based on global MHD simulation and spacecraft measurements, *J. Geophys. Res.*, *117*, A10210, doi:10.1029/2012JA017901.

Walt, M. (1964), The effects of atmospheric collisions on geomagnetically trapped electrons, *J. Geophys. Res.*, *69*(19), 3947–3958.

Walt, M., and T. A. Farley (1976), The physical mechanisms of the inner Van Allen belt, *Fundam. Cosmic Phys.*, *2*, 1–110.

Yu, Y., J. Koller, S. Zaharia, and V. Jordanova (2012), L^* neural networks from different magnetic field models and their applicability, *Space Weather*, *10*, S02014, doi:10.1029/2011SW000743.

Zhao, H., and X. Li (2013), Inward shift of outer radiation belt electrons as a function of *Dst* index and the influence of the solar wind on electron injections into the slot region, *J. Geophys. Res. Space Physics*, *118*, 756–764, doi:10.1029/2012JA018179.